STATIC FATIGUE OF HI-NICALON™ S FIBER TOWS AT 500°C IN AIR AND IN SILICIC ACID-SATURATED STEAM

Thesis

Richard J. Reinink, Captain, USAF
AFIT-ENY-MS-21-M-315

DEPARTMENT OF THE AIR FORCE
AIR UNIVERSITY

AIR FORCE INSTITUTE OF TECHNOLOGY

Wright-Patterson Air Force Base, Ohio

AFIT-ENY-MS-21-M-315

STATIC FATIGUE OF HI-NICALON™ S FIBER TOWS AT 500°C IN AIR AND IN SILICIC ACID-SATURATED STEAM

THESIS

Presented to the Faculty

Department of Aeronautical and Astronautical Engineering

Graduate School of Engineering and Management

Air Force Institute of Technology

Air University

Air Education and Training Command

In Partial Fulfillment of the Requirements for the

Degree of Master of Science (Materials Science)

Richard J. Reinink

Captain, USAF

March 2021

AFIT-ENY-MS-21-M-315

STATIC FATIGUE OF HI-NICALON™ S FIBER TOWS AT 500°C IN AIR AND IN SILICIC ACID-SATURATED STEAM

Richard J. Reinink

Captain, USAF

Approved:

_____	_____
Marina Ruggles-Wrenn, PhD (Chairman)	Date
_____	_____
Randall Hay, PhD (Member)	Date
_____	_____
Eric Jones, PhD (Member)	Date

Abstract

Recent developments in aerospace propulsion systems, as well as the emerging interest in hypersonic air vehicles has emphasized the need for new materials which can withstand extreme service environments. Such hostile environments frequently involve extremely high temperatures and the presence of steam. The leading candidates for the structural components expected to operate in extreme service environments are SiC-based ceramic matrix composites (CMCs). However, before these materials can be used in actual applications, their structural integrity and environmental durability must be assured. A thorough understanding of the performance of the SiC constituents of the composite is critical to ensuring safe and reliable use of the SiC-based CMCs in structural applications. When a CMC component is subjected to thermomechanical loads in an aggressive environment during service, surface cracks form. High-temperature steam can be a major component of the service environment. As steam penetrates cracks in the SiC matrix, it becomes saturated with silicic acid, ($SI(OH)_4$). The saturated steam travels through the composite and attacks the oxidation prone SiC fibers. The interaction between the reinforcing Hi-Nicalon™ S SiC fibers and the $Si(OH)_4$-saturated steam is not fully understood. Understanding the nature and mechanisms of the stressed oxication of the reinforcing SiC fibers is essential to predicting long-term durability and assuring structural integrity of SiC/SiC CMCs. This experimental research effort focused on static fatigue of Hi-Nicalon™ S fiber tows at 500°C in air and in silicic acid-saturated steam. The fiber tows were composed of approximately 500 individual fiber filaments with an average diameter of 12 μm. The applied stress ranged from 3.6 MPa to 1350 MPa. Tests

were performed in both air and silicic acid-saturated steam. Test run-out was defined as 100 hours under loading, and was achieved in every test. Both primary and secondary deformation regimes were observed, and steady-state strain rates were found for each test. The effects of applied load and test environment on static fatigue performance of the SiC fiber tow are discussed.

Acknowledgements

First and foremost, I need to thank my advisor and instructor Dr Ruggles-Wrenn for assisting me throughout my time at AFIT. From teaching multiple courses with direct thesis application to assisting with the administration requirements and getting me oriented with the lab equipment and testing process, Dr Ruggles-Wrenn was a vital component to accomplishing what I did. I would also like to thank C.N. for being extremely gracious and flexible when outside circumstances forced me to change thesis directions and hold concurrent fiber testing with her. Her assistance with troubleshooting, along with R.M., was also invaluable. Our lab technicians also contributed tireless help and crucial experience in the lab. Without their expertise in diagnosing equipment troubles and their patience with C.N. and myself as we continually brought new issues to them, testing could not have been accomplished. Finally, I would like to thank my wife for being patient with my frequent trips at odd times to the laboratory and the adjustments she made to her daily work schedule to allow me to attend class virtually for much of the past year.

Table of Contents

List of Figures

List of Tables

STATIC FATIGUE OF HI-NICALON™ S FIBER TOWS AT 500°C IN AIR AND SILICIC ACID-SATURATED STEAM

I Introduction

History has long been understood in terms of the materials from which the civilizations construct their most advanced technology – typically weapons and tools. From the Stone Age to the Bronze Age and to the Iron Age, the materials available to a society have shaped our understanding of the society. Our current age has been given various descriptive names, such as the Plastic Age and the Silicon Age, but one name which has merit alongside the others is the Composite Age.

A composite material is an engineered material [1] which contains two or more distinct phases within a continuum [2]. In general terms, these phases are combined in a way such that the composite material has more desirable properties than either of the constituent phase materials would by themselves. One industry which has seen widespread adoption of composite materials and has been a driving force in their development is the aerospace industry. The stringent demands placed on the materials used in air and space vehicles – which must all be strong, tough, stiff, and lightweight – are demands which composite materials are uniquely well-suited to meet.

Examples of early composite materials are straw-reinforced bricks and bone-and-wood bows from the Ancient World and iron-reinforced concrete from the nineteenth century [3]. The middle of the twentieth century, however, produced a materials availability revolution on par with the opening of copper mines on Cyprus around 3,000 BCE [4]. By the 1950s, fiber production had advanced to the point that composite

materials had begun being used on aircraft, missiles, and electrical components. Carbon fiber composites came along in the 1960s, followed by metal-matrix composites in the 1970s. The 1970s is also the time that commercial use of composite materials grew exponentially, until composites could be found regularly used in fields as disparate as aerospace, biomedical, and sporting goods [3].

In the aerospace field, ceramic-matrix composites (CMCs) are of particular interest. Ceramics boast many desirable properties for aerospace applications, such as high strength, hardness, temperature resilience, chemical inertness, and wear resistance combined with a lower density than metals or polymers [2]. However, their serious downside is that they are prone to catastrophic failure due to their inability to support significant amounts of plastic deformation. Any efforts to modify the ceramic itself would be counterproductive: the microstructure and bonding that prevent the accumulation of plastic deformation prior to failure are simultaneously the source of the stiffness, strength, hardness, and temperature resilience to be preserved. After the advent of filament winding in 1946 [3], it became possible to incorporate fibers into the ceramic material to achieve the desired properties. Fibers reinforcing the ceramic matrix increase the material's toughness by deflecting crack propagation, bridging cracks that do spread, and exerting a traction force counteracting the opening force of the cracks [2].

Suitable applications for CMCs include structural components as well as internal engine parts. The lightweight nature of CMCs is vital for modern aircraft structures, which rely on lowering their weight for increases in power, range, speed, carrying capacity, and/or altitude. In addition, CMCs are finding increasing use in environments too extreme for metals to be used, such as in aircraft engine combustion chambers. The

ceramic matrix is extremely temperature resistant, allowing the fiber-reinforced composite material to maintain its mechanical properties at temperatures which would cause metals to exhibit deterioration of their mechanical material properties. In addition to their temperature resilience, CMCs also tend to have good resistance to aggressive environments found inside combustion chambers, which produce steam as a part of their combustion reaction.

II Background

2.1 Monolithic Ceramics

The utility and drawbacks of ceramic materials has been well understood since ancient times. While not necessarily discussed in these terms, civilizations across the world have utilized ceramic materials for its thermal resilience, strength, hardness, and corrosion resistance by creating pottery cookware and dishes. At the same time, they understood the fragility inherent in its brittle nature, as no weapons or heavy tools such as picks or shovels have been found made of any ceramic material. Despite its strength, ceramic materials lack toughness and have therefore been judged lacking for aggressive use throughout human history.

The reason for the remarkable strength, stiffness, and resilience of ceramic materials has to do with the atomic bonding of its constituent elements. Being composed of nonmetals, ceramics are bonded with ionic and/or covalent bonds. These bonds are extremely strong, giving the material high stiffness and strength [2, 5]. However, due to their strength, they are very stiff bonds and cannot flex to support significant amounts of elastic or plastic deformation. These strong bonds are also the reason for ceramics' ability to withstand extreme temperatures and aggressive environments without significant degradation.

The brittle nature of ceramics is a serious drawback to their utilization in aerospace applications. Since they do not display any deformation prior to failure, ultimate failure appears suddenly and catastrophically as cracks propagate rapidly through the material. They also tend to perform significantly worse under tensile and

impact loading [2], which are loading cases they must endure to be utilized in aerospace vehicles. While ceramics perform very well under high temperatures, they suffer from not handling rapid thermal change (thermal shock) well, which can also lead to sudden catastrophic failure [2].

The reason for the sudden failures in monolithic ceramics is the stiff, strong atomic bonding. As energy in the form of loading is applied to the material, ceramics have nowhere to dissipate that energy except via fracturing. Metals and polymers, by contrast, are able to lower their internal energy by plastically deforming or through production of "process zones" in the vicinity of internal flaws [5]. As ceramics do not yield, they lack these energy dissipation processes and have very low fracture toughness values, as seen in Table 1.

Table 1. Typical Fracture Toughness Values, reproduced from [2]

Material	K_{IC} (MPa $m^{1/2}$)
Polymers	
Polyethylene	1-2
Nylon	3
Epoxy, Polyester	0.5
Metals	
Pure metals (copper, nickel, aluminum)	20-50
Aluminum alloys	20-50
Low carbon steel	50
Cast iron	4-10
Ceramics	
Sodalime glass	0.5-1
Magnesium oxide	3
Alumina	1-3
Silicon oxide	2-4
Silicon nitride	3-5

Physically, this means that ceramics are very intolerant of any defects present in the microstructure. Without being able to dissipate energy through plastic deformation, any defects present will continue to grow until some defect reaches a critical size. With the elimination of all defects being an impractical method of resolving this issue, the synthesis of fiber- or whisker-reinforced composites has proven to be able to increase a ceramics' fracture toughness [5].

2.2 Ceramic Matrix Composites (CMCs)

A common method of increasing a ceramic materials' toughness is to reinforce it with fibers. As the essential problem leading to a ceramic's brittleness is a lack of energy-dissipation mechanisms, fiber reinforcement is carefully tuned to allow this to happen. Somewhat counter-intuitively, the fibers added to these brittle ceramics are themselves brittle fibers, but when properly implemented they serve to introduce quasi-ductility to the composite material as a whole, improving toughness and providing a less catastrophic failure mode, as seen in Figure 1.

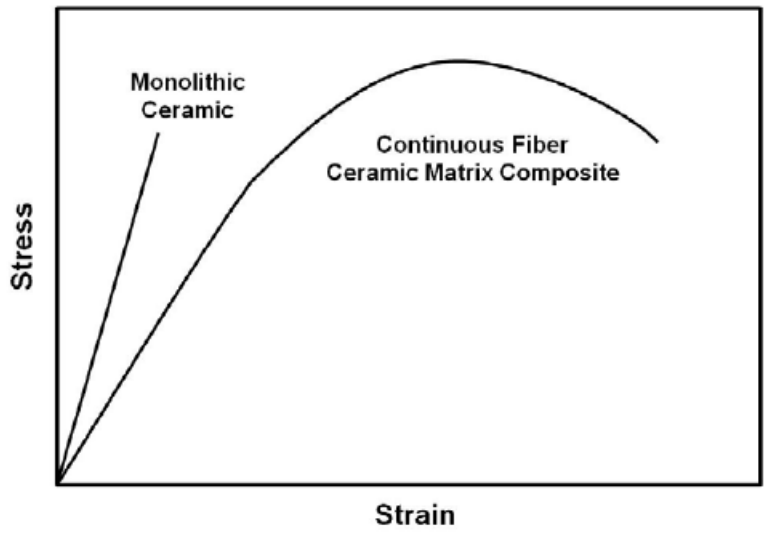

Figure 1. Representative stress-strain curve for monolithic ceramic vs CMC. Reproduced from Armani [6].

The key to the implementation of the fibers is the interface between the matrix and fiber. While the interface bond needs to be strong enough to ensure the material acts as a continuum, it can't be too strong [7]. A sufficiently weak interface between the strong but brittle matrix and fiber allows energy to be diverted from crack propagation. This occurs in several ways: crack deflection and fiber bridging will be discussed in more detail [2]. This weak interface is itself accomplished in three main paths: either by coating the fibers in a material to provide the weak interface, utilizing a porous matrix which will not bond tightly to the fiber, or by coating the fibers in a material destroyed during the composite's final synthesis, leaving a void between the fibers and matrix [8].

The first energy dissipation method is simple crack deflection. As the crack front propagates through the matrix and reaches the fiber, it will divert through the weak interface material instead of traveling through the relatively stronger matrix. As these crack fronts propagate around and along the fibers, they are not working to advance the

crack through the composite as a whole. In addition, this serves to increase the surface area of the fracture surface, requiring more energy to advance the crack front [5].

Fiber bridging is the most impactful method of toughening, and the reason fiber reinforcements are chosen. If the fiber-matrix interface is sufficiently weak, any crack front propagating through the matrix will deflect around the fibers, leaving them intact. As the crack opens, the intact fibers will bridge the crack, serving to oppose its opening. Two methods are modeled for this phenomenon: debonding and frictional sliding [5]. In the debonding model, the fiber and matrix are allowed to move relative to each other because energy is dissipated in breaking the weak bonds all along the bridging fibers. Even as the crack widens away from the crack front, energy is continually required to further debond the fiber and matrix, allowing the matrix crack to open wider [2]. An alternate model views the relative motion of the matrix and fiber as the crack widens as producing a sliding traction force [5]. As this traction force necessarily acts against the motion of the opening crack, it serves to oppose the progress of the crack front through the CMC. Fiber bridging is also effective at elevated temperatures, as the fibers themselves are made of the same temperature-resilient ceramics as the matrix.

An improperly designed CMC with a strong fiber-matrix interface fails to take advantage of these toughening methods. Instead, its fracture toughness is dependent solely on the relative toughnesses of its constituent materials and little if any improvement is seen over a monolithic ceramic. Effective implementation of the above methods can raise the fracture toughness of a CMC to ~20 MPa $m^{1/2}$ [5] despite the weakness of the fibers themselves – Hi-Nicalon™ S fibers boast a fracture toughness of only 1.4 MPa $m^{1/2}$ [9].

2.3 Silicon Carbide (SiC) Fibers

While silicon carbide has been in production for over a century, silicon carbide fibers were not produced until the 1970s in Japan by Nippon Carbon Co. Ltd. and Ube Industries Ltd. First generation fibers were plagued by large amounts of oxygen in the form of amorphous silicon oxycarbide phases. These phases, a result of curing the fibers under oxygen during synthesis, would decompose above 1100°C, leading to significant strength degradation. Second-generation fibers were produced which eliminated nearly all the oxygen either by replacing oxygen curing with electron beam curing, or by utilizing zirconium instead of the oxygen for curing. These fibers displayed much improved thermal stability over the first generation, however they had excess carbon which reduced their resistance to oxidation and creep deformation. Third-generation fibers, such as Hi-Nicalon™ S, were then created to eliminate this excess carbon and bring the SiC into nearly stoichiometric proportions. The Hi-Nicalon™ S fibers are fabricated through melt spinning, electron beam curing, anaerobic pyrolysis, and high-temperature thermal treating under hydrogen [7].

The microstructure of the SiC fibers changed drastically through the generations along with the processing technique and elemental makeup. First- and second-generation fibers were composed of an amorphous SiC_xO_y structure, with small SiC grains embedded. From the first to the second generation, processing improvements had resulted in increasing the size of the SiC grains, lowering the amount of amorphous SiC_xO_y present. Third generation fibers, by contrast, are composed entirely of small SiC grains, thereby creating a far more resilient microstructure [10, 11].

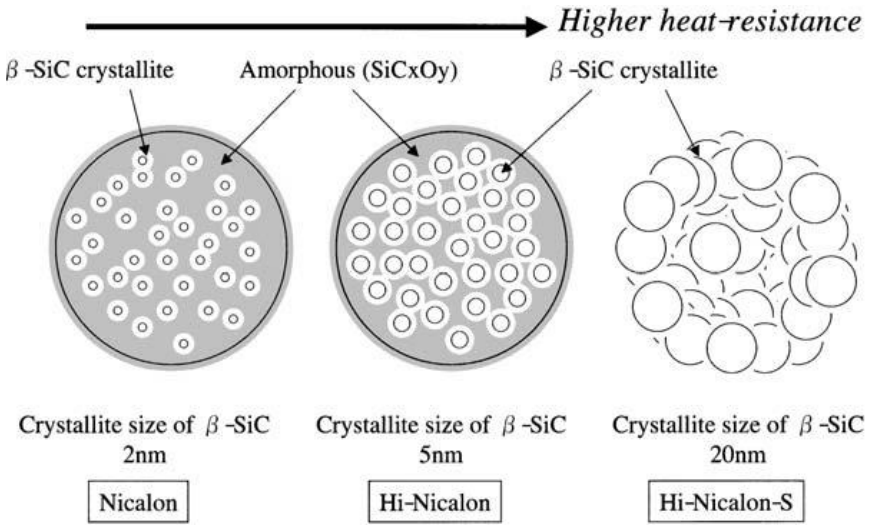

Figure 2. Microstructure development of Nicalon™ fibers. Reproduced with permission from Springer Nature [10], pg 118 Figure 9, copyright © 2005 by Springer-Verlag Berlin Heidelberg.

2.3 Creep in Ceramics

Creep deformation occurs when a material under constant stress accumulates strain over time [12, 13]. The physical mechanisms for this deformation are varied and depend on the particular microstructure of the material being evaluated. In general, however, creep deformation rates will increase with temperature and will also increase in aggressive environments, such as the oxidizing environment found in propulsion systems of air vehicles. For crystalline materials such as metals, creep needs to be taken into account when the temperature is between 30% and 60% of the materials melting temperature [12]. Engineering alloys exhibit wide variability in their resistance to creep deformation with respect to temperature, while crystalline ceramics exhibit greater creep resistance with respect to temperature.

A notional strain-time plot during constant engineering stress is shown in Figure 3.

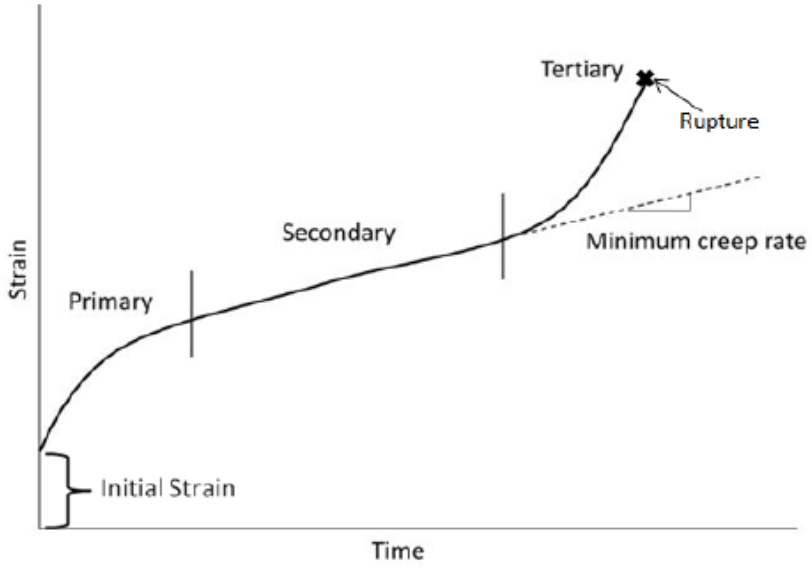

Figure 3. Creep deformation regimes. Reproduced from Robertson [14].

Creep response plots are characterized by three regimes. Primary creep consists of the elastic response, which can be idealized as happening instantaneously, with the creep response slowing over time until it reaches a steady creep rate. This steady-state creep rate is the secondary creep regime, and generally consists of the bulk of the material's creep response. As the material steadily deforms over time, the distinction between true stress and engineering stress needs to be made. If the engineering stress is to be held constant, the load is not varied as the material deforms and the cross-sectional area decreases. In this case, the material moves into the tertiary creep regime, where the strain rate increases in an unstable manner until ultimate material failure. Ceramic materials, however, do not produce significant amounts of plastic strain and can be represented as having a constant true stress applied. When true stress is held constant, the steady-state creep deformation rate will continue until ultimate material failure is reached. The region of interest for the purpose of material characterization is the region of steady-state creep

response, and the quantity of particular interest is the slope of the strain response: the minimum strain rate of the material while undergoing creep.

The physical mechanisms for creep deformation vary not only between classes of materials, but within classes of materials and within individual materials themselves. A single material can exhibit various creep mechanisms for unique combinations of stress, temperature, and environment. Crystalline materials are of particular interest to the Air Force as the both the fiber and matrix materials under consideration for high-temperature applications for these composites are of crystalline microstructure. CMCs commonly show two types of physical mechanisms: diffusional flow and grain boundary sliding [12].

Diffusional flow is caused by the movement of vacancies in the material while under stress. These vacancies, generally located at grain boundaries, move from grain boundaries oriented normal to the load to grain boundaries oriented parallel to the load. As these vacancies move, their lattice locations are back-filled by the atoms they are displacing, and the net result is a shift in the shape of the individual grain. On a macroscopic scale, this results in the elongation of the material in the direction of loading, and a contraction in the normal directions. If these migrating vacancies diffuse through the crystal lattice, it is referred to as Nabarro-Herring creep. If, however, the vacancies travel around the grain via the grain boundaries, it is called Coble creep. This creep mechanism is sensitive to grain size, as the number of grain boundaries increases when grain size decreases.

A subset of diffusional flow is grain boundary sliding. This occurs when the vacancies have accumulated along the boundaries parallel to the stress flow. As the grains

grow in the direction of loading, they can move relative to each other now that there are a large number of vacant lattice sites between them. Interstitial or impurity atoms can be doped into the grain boundaries in order to pin them in place and mitigate this creep mechanism.

The general equation for creep deformation in crystalline materials is given in Equation 1 [12]:

$$\dot{\varepsilon} = \frac{A_2 \sigma^m}{d^q T} e^{-Q/RT} \tag{1}$$

In this equation, σ is the applied stress, d is the average grain diameter, Q is the activation energy required for molecular motion to occur, R is the universal gas constant, and T is the absolute temperature. A_2, m, and q are obtained experimentally for the specific material and creep mechanism.

For ceramic materials, Equation 1 can be further refined, and produces the form seen in Equation 2 [15].

$$\dot{\varepsilon} = B \frac{D\mu b}{kT} \left(\frac{b}{d}\right)^p \left(\frac{\sigma}{\mu}\right)^n \tag{2}$$

In this form, B is an experimental constant, D is the diffusion coefficient, μ is the shear modulus, b is the Burger's vector magnitude, k is the Boltzmann constant, T is absolute temperature, d is the average grain diameter, σ is the applied stress, p is the grain size power law exponent, and n is the stress law power exponent.

The particular creep mechanism can be determined experimentally by calculating the value of p and n, and comparing to a table of universal constants, Table 2.

Table 2. Creep mechanisms in fine-grained polycrystalline ceramics. Reproduced from Armani [6].

n stress exponent	p grain size exponent	Mechanism
1	2	Diffusional creep through lattice (Nabarro-Herring creep)
1	3	Diffusional creep along grain boundaries (Coble creep)
2	1	Grain boundary sliding and interface-reaction controlled creep
4	3	Grain boundary sliding and cavity growth
3-5	0	Dislocation creep: 3-glide controlled, 5-climb controlled
>5		Cavity growth controlled creep

Consistent with the physical creep mechanism, both Nabarro-Herring and Coble creep are more sensitive to grain size than the applied stress. Grain boundary sliding has variable dependence on grain size depending on whether the vacancies accumulated at the grain boundaries via the Nabarro-Herring or Coble creep mechanisms.

III Experimental Method

3.1 Fiber Tows

This experimental research effort examined static fatigue of Hi-Nicalon™ S fiber tows at 500°C in laboratory air and silicic acid-saturated steam. The fiber tow specimens used in this effort were fabricated from the same fiber spool as those used in the previous research efforts of Steffens [16], Shillig [17], Piper [18], Robertson [14], Mitchell [19], Kroeger [20], and Gumucio [21]. Material properties of the Hi-Nicalon™ S fibers are summarized below in Table 3.

Table 3. Typical Hi-Nicalon™ S Properties, [22, 23].

Density (g/cc)	2.85 - 3.10
Oxygen content (wt%)	0.2 - 0.8
C/Si Atomic Ratio	1.05
Tensile Strength (GPa)	2.6 - 3.1
Tensile Modulus (GPa)	380-420

The fiber tow consisted of 500 individual filaments with an average diameter of 12 μm [22]. Assuming all individual filaments remained intact, the fiber tow has an average diameter of 5.7×10^{-8} m^2.

Test specimens were created from 18-inch lengths of fiber tow by utilizing the fiberglass tab method pioneered by Steffens [16]. Details of the specimen preparation process are included in section 3.4.

3.2 Experimental Equipment

The testing was conducted in the AFIT Advanced Aerospace Materials Laboratory, at the testing facility initially developed by Armani [6] and used by Steffens [16] and Shillig [17]. The original station, designed by Armani, was designed to test fiber tows at elevated temperatures in air and pure steam [6]. This testing was accomplished by hanging a specimen from a fixed mounting position with a dead weight attached to its lower tab and its gauge section heated to the desired temperature.

When used by Shillig to test SiC fiber tows, it was discovered that pure steam was producing uneven oxidation on the fiber tows [17]. The lower portion of the fibers, nearest the steam entry point, displayed signs of aggressive active oxidation. In contrast, the higher portions of the fiber showed signs of passive oxidation. The inference drawn was that the steam was leaching silicon from the fibers when it entered the test chamber, and became saturated by the time it reached the top of the chamber. In order to provide consistent oxidation across the entire gauge section, the station was modified by Robertson to deliver steam already saturated with silicic acid [14]. In addition to being saturated with silicic acid, the steam also delivered to the test chamber already at the target test temperature. This re-designed facility was used by Piper [18], Mitchell [19], Kroeger [20], and Gumucio [21] in their research efforts. Of primary importance in the new test facility is the ability to deliver pre-heated steam at the target test temperature to the test chamber.

The test specimen was attached at both ends to hooks through the holes in its primary tables. The upper hook was stationary and mounted to a swing arm connected to an MTS tabletop machine. The lower hook was connected to a Schaevitz M12-30 35

linear variable differential transformer (also called a linear variable displacement transducer, or LVDT), which provided displacement measurements to an MTS FlexTest 40 digital controller. Hence, test specimen elongation is measured outside the furnace with an LVDT attacked to the bottom tab of the fiber tow specimen. The dead weight, used to apply constant tensile load to the test specimen, is attached to the rod extending from the bottom of the LVDT.

A compact two-zone resistance heated furnace (Model 653.03A, MTS Systems Corporation, Eden Prairie, MN) with two temperature controllers (MTS 409.83) provide the high temperature environment. This compact furnace included four silicon carbine heating elements and two R-type thermocouples controlling in two zones: an upper and a lower. Each zone contained a left and right heating element and a thermocouple. An alumina susceptor (a tube with capped ends) designed to fit inside the furnace was used in all tests. The gauge section of the fiber tow specimen was located inside the susceptor, while the specimen ends passed through slots in the top and bottom end caps of the susceptor. The susceptor was used to achieve a more uniform and repeatable temperature distribution along the fiber tow. Additionally, when testing in saturated steam, the alumina susceptor protected the heating elements from the silicic acid-saturated steam.

For testing in steam, steam was generated using deionized water and a Micropyretic Heaters International HGA-S steam generator. The deionized water was transported from covered storage barrel to the steam generator by a Cole Parmer 7518-10 peristatic pump. Upon exiting the steam generator, the steam passed through two CX1300 heating units equipped with custom designed heating coils manufactured by I Squared R Element Company and encased in RATH KVS 174/400 insulation. Temperature control

for the heating units was accomplished with an IBPAN controller. While passing through the heating units, the steam traveled through an alumina cylinder loosely packed with silica wool in order to saturate the steam with silicic acid. Upon exiting the heating units steam entered the susceptor through a feeding tube.

External insulation blocks were placed on top of the furnace to minimize heat loss through the seam between the furnace halves and the opening cut for the specimen. Insulation blocks were also placed around the alumina tube carrying the saturated steam from the heating units to the susceptor. Finally, loose silica insulation was layered over the heating units assembly.

A step-by-step procedure for starting up the dormant testing station and ensuring all equipment functions properly is included in the appendix.

3.3 Temperature Profiles

Prior to testing, temperature profiles were established to (1) confirm the temperature controller settings used for the tests, and (2) to determine the effective length later used in strain calculations. The temperature profiles were resolved by inserting a K-type thermocouple into the test chamber, then measuring and recording temperatures at various points along the length of the test chamber. Temperature measurements were made starting at the bottom or 40 mm below the center-point of the susceptor to the top or 40 mm above the center-point of the test chamber. Prior to taking temperature measurements, the test chamber was allowed to soak at the target test temperature for 45 minutes when generating a temperature profile in air, and 60 minutes when generating a temperature profile in steam. The longer soak period for steam testing was chosen

because of the added complexity of running multiple connected temperature feedback control systems – two in the furnace and one for the steam heating coils.

When obtaining the profile in steam, care was taken to set the steam's heating coils such that the temperature of the steam upon entering the test chamber was 500°C. These settings were found by inserting the steam outlet tube into the empty test chamber with the furnace at the desired temperature settings. Through iteration, the proper temperature settings for the furnace and the steam heating coils could be found. The temperature profiles determined for testing in air and steam are shown in Figures 4 and 5, respectively.

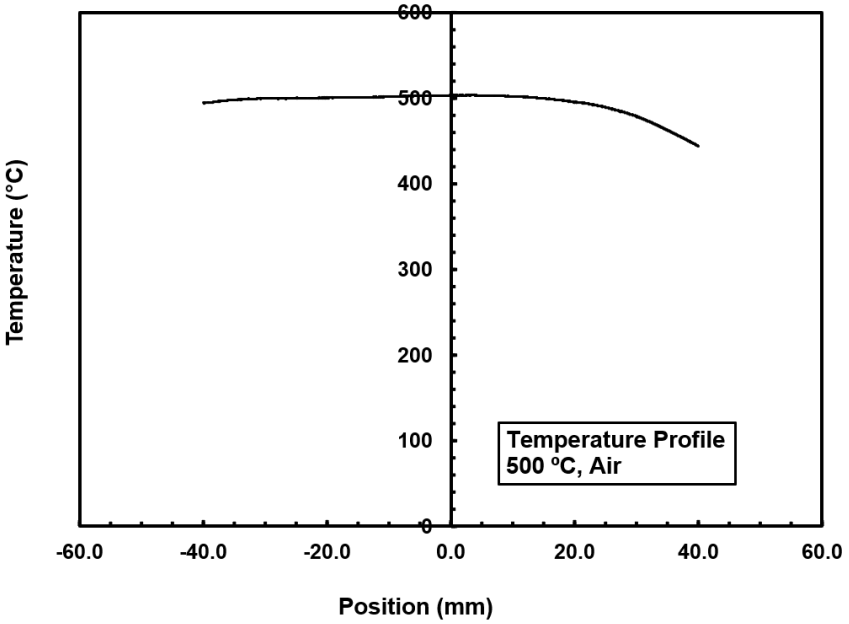

Figure 4. Temperature profile in air

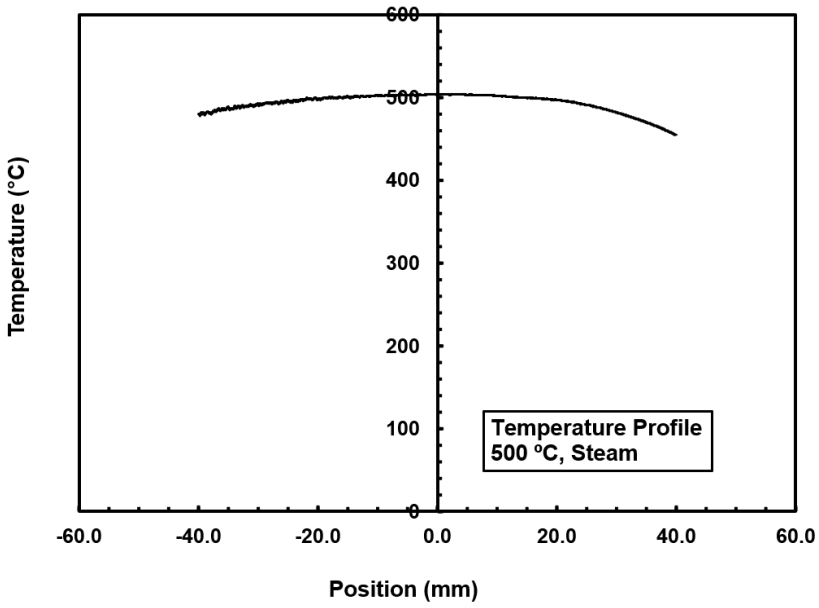

Figure 5. Temperature profile in saturated steam

3.4 Specimen Preparation Procedure

The specimens were prepared using the procedures developed by Steffens [16]. The specimens were fabricated from 18-inch lengths of Hi-Nicalon™ S fiber tow with fiberglass tabs at both ends to allow the fiber to be mounted to the hooks in the testing station. Three fiberglass tabs were used at each end to ensure sufficient adhesion to the fiber tow. The primary tab was the largest, measuring 1.5 inches by 1 inch, and had a 0.25-inch-diameter hole punched into its centerline to mount to the hooks. Atop this tab, the fiber tow was carefully aligned with the tab's centerline and affixed using a drop of Dubble-Bubble two-part adhesive. Directly atop the drop of adhesive was placed the secondary tab, which measured 1 inch by 1 inch. When the adhesive was set, the fiber tow was carefully doubled back over itself and affixed atop the secondary tab by another drop of adhesive. Atop this adhesive was placed the tertiary tab, which measured 0.75 inch by 0.75 inch. The tab configuration is shown in Figure 6, and the overall steps can be seen in Figure 7.

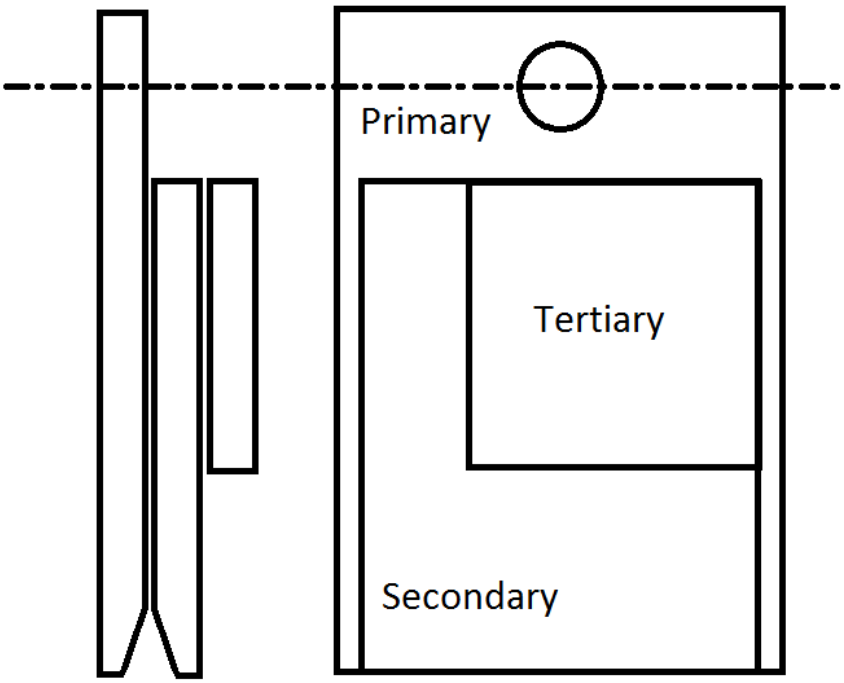

Figure 6. Specimen tab stack-up. Reproduced from Mitchell [19].

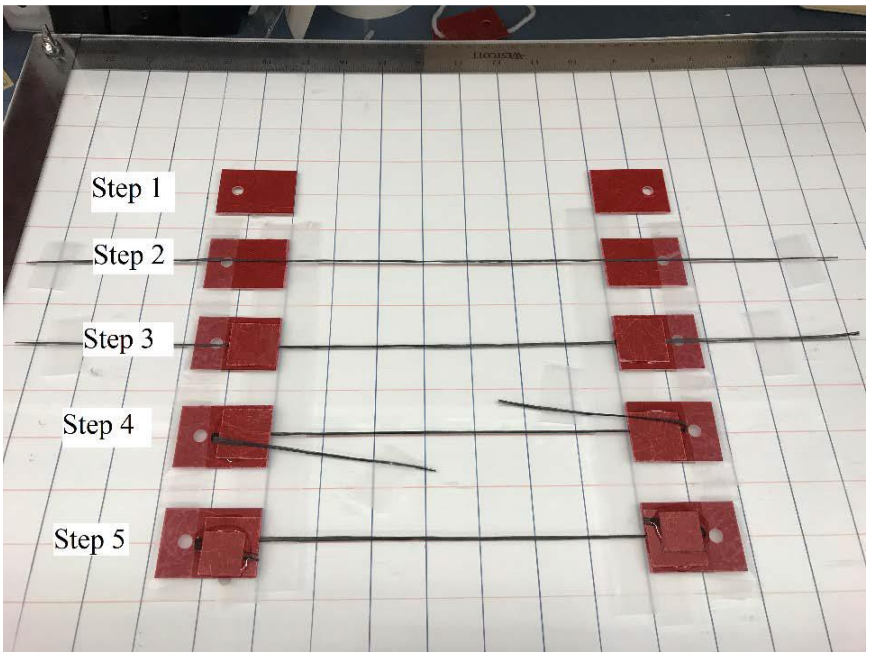

Figure 7. Test specimen preparation process. Reproduced from Gumucio [21].

The distance between the tabs measured 7 inches. Combined with the lengths of the tabs themselves, the distance between the mounting holes on either end measured 9

inches. Specimen preparation was done on atop a board marked with grid lines to ensure both proper specimen alignment and the capability to fabricate multiple specimens simultaneously. To ensure proper alignment was maintained, both the fiber tows and fiberglass tabs were fixed in their positions to the grid board with tape prior to adhesive being applied, and while the adhesive was curing.

After fabrication was complete and the adhesive had fully cured, the excess fiber tow was trimmed and the specimens were labeled on their tertiary tabs. After careful removal from the grid board, the specimens were stored in enclosed, hard-sided containers until use.

3.5 Test Procedure

The first step in conducting the dead-weight creep test was to identify the weights needed to produce the desired stress and balance them underneath the LVDT. To select the amount of weight to load, it was assumed that all 500 filaments in the fiber tow were intact. Using the cross-sectional area obtained by that assumption and subtracting the weight of the lower mounting hook and rod passing through the LVDT, the stack of weights was selected. Plates were chosen to fit the height of the total stack to the space available between the end of the LVDT and the mounting washer. With the use of an elevator and a rigid loop sized to the length of the specimens hung from the upper mounting hook, the weights were balanced and readied to be hung from the specimen itself.

Next, the selected specimen was suspended from the upper hook and the susceptor was closed around the gauge section, extreme care being taken not to contact the susceptor end caps with the exposed fiber. With the susceptor in place, the furnace

was closed and brought to the desired temperature over a period of two minutes. After a soaking period of 45 minutes, the weights were hung from lower tab's mounting hole and the test commenced. At the conclusion of the test the furnace temperature was lowered to room temperature over a period of 10 minutes and the weights were detached from the specimen. When the furnace reached room temperature, the specimen was removed from the susceptor, care being taken again not to allow contact between the fiber and the susceptor end caps.

For steam tests the water pump, steam generator, and heating coils were turned on and given two hours for the steam to reach the desired temperature. During this time, the weights were readied as in the air tests. With the steam at the test temperature, the steam outlet tube was inserted through a pair of holes in the furnace insulation blocks and the susceptor wall. With the steam being inserted into the susceptor, the furnace was heated over a period of five minutes and allowed to soak for one hour. These longer soak and ramp-up periods were again chosen due to the complexity added to the system by the steam. At the end of this time, the weights were loaded and the test proceeded in the manner of the air tests.

IV Results

4.1 Temperature Profiles

Temperature profiles were obtained along the centerline of the susceptor prior to testing in air and team for two reasons. First, having a robust temperature profile ensures the temperature of the fiber will be the desired test temperature. Second, the temperature profile curve allows the calculation of an effective length necessary for strain calculations. The effective length is necessary because even though the majority of the susceptor is at 500°C, there are significant temperature gradients at both the top and bottom of the susceptor. The fiber passing through these regions will experience some degree of temperature-enabled deformation, but not to the degree of the central hot portion. Creep from the portions of the fiber at room temperature outside the furnace is considered negligible for this research. To most thoroughly account for the temperature effect on creep strain, however, the contributions of the hot zone and the gradient zones must be considered.

Some researchers have found an effective length by selecting the subjectively flattest portion of the temperature profile. Due to the inherently imprecise nature of this method, this research calculates the effective length using the approach employed by Armani [6] and summarized below.

Consider a specimen of length 2L undergoing creep with the zero point at the center of the specimen. This specimen will experience creep strain accumulation from every point along the specimen's length, no matter each point's temperature. The measured creep strain and creep strain rate can be calculated as follows:

$$\varepsilon_m = \frac{\Delta l}{2L} = \int_0^t \dot{\varepsilon_m} dt \tag{3}$$

$$\dot{\varepsilon}_m = \frac{\dot{\Delta} l}{2L} = \frac{1}{2L} \int_{-L}^{L} \dot{\varepsilon} dl \tag{4}$$

If only the strain at the center of the specimen is considered, it can be calculated by taking the integral of the center point's strain rate, or by dividing the total deformation by a quantity known as the effective length. The center point's strain rate can also be expressed in terms of this effective length.

$$\varepsilon_0 = \int_0^t \dot{\varepsilon_0} dt = \frac{\Delta l}{2L_{eff}} \tag{5}$$

$$\dot{\varepsilon}_0 = \frac{\dot{\Delta} l}{2L_{eff}} = \frac{1}{2L_{eff}} \int_{-L}^{L} \dot{\varepsilon} dl \tag{6}$$

The ratio of Equations 4 and 6 can be written as:

$$\frac{\dot{\varepsilon_m}}{\dot{\varepsilon_0}} = \frac{2L_{eff}}{2L} \tag{7}$$

Due to the choice of applying a dead-weight load to the specimen, and the fact that the specimen's temperature is a function of location, a general power-law creep equation can be applied:

$$\dot{\varepsilon} = A\sigma^n \exp\left(\frac{-Q}{RT(l)}\right) \tag{8}$$

When combined with equations 7, 4, and 6, the power-law equation becomes:

$$\frac{\dot{\varepsilon_m}}{\dot{\varepsilon_0}} = \frac{1}{2L}\int_{-L}^{L} \exp\left(\frac{-Q}{R}\left(\frac{1}{T(l)} - \frac{1}{T_0}\right)\right) dl \tag{9}$$

Given that the temperature profile tests yield columns of data, it can be convenient to express the above equation as a summation of length increments rather than an integral. In the below equations, the length increments are h, where L = hk and k is an integer.

$$\frac{\dot{\varepsilon_m}}{\dot{\varepsilon_0}} = \frac{1}{2k}\sum_{i=-k}^{k} \exp\left(\frac{-Q}{R}\left(\frac{1}{T_h} - \frac{1}{T_0}\right)\right) \tag{10}$$

Having calculated this ratio from the temperature profile data, the effective length can be found from equation 11:

$$2L_{eff} = 2L\left(\frac{\dot{\varepsilon_m}}{\dot{\varepsilon_0}}\right) \tag{11}$$

Using the creep activation energy value of 177 kJ/mol for Hi-Nicalon™ S fibers [9], the standard handbook value for the universal gas constant R, and the data from the temperature profile tests in air and saturated steam, the effective lengths for 500°C in both air and saturated steam can be calculated.

Table 4. Summary of Effective Lengths at 500°C

	Air	Silicic Acid-Saturated Steam
Effective Length (mm)	64.01	61.15

These effective lengths presented in Table 4 will be used in Sections 4.2 and 4.3 to calculate strains produced in each of the tests.

4.2 Static Fatigue in Air

Tensile static fatigue tests in air were performed at 500°C for applied stresses ranging from 3.5 MPa to 1300 MPa. The results are summarized in Table 5 and Figure 8. For this research, static fatigue runout was defined as 100 hours under load.

Table 5. Summary of Tensile Static Fatigue Tests of Hi-Nicalon^{TM} S in Air at 500°C

Specimen	Applied Stress (MPa)	Lifetime (hr)	Steady-state Creep Rate (1/s)	Total Strain (%)
R-01	3.6	100	9.53×10^{-11}	0.00754
R-14	936.9	100	8.14×10^{-10}	0.258
R-16	1156.0	100	3.07×10^{-9}	0.231
R-18	1257.1	100	2.61×10^{-9}	0.455
R-19	1300.0	100	1.29×10^{-9}	0.237

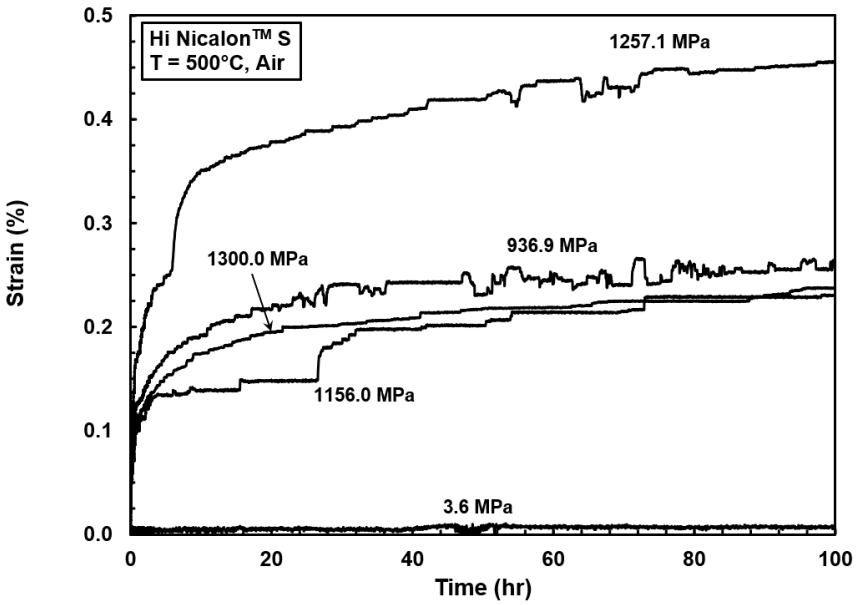

Figure 8. Strain vs time curves obtained for Hi-Nicalon^{TM} S fiber tows at 500° C in air

By focusing on the first five hours, we note an initial period of transient strain vs time behavior followed by a steady-state strain vs time behavior in each test. Typically, transient behavior transitions to the steady-state behavior by the end of the first hour under load.

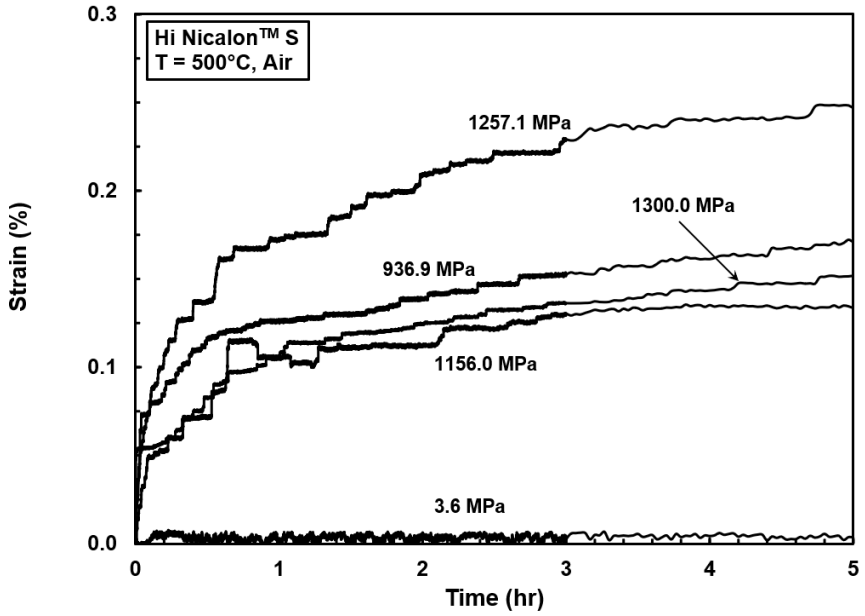

Figure 9. Strain vs time curves obtained for Hi-Nicalon™ S fiber tows at 500°C in air. The time scale is truncated to highlight strain vs time behavior during the first 5 h of the test.

It is recognized that the mechanism behind strain accumulation in these tests is progressive failure of the individual filaments (or groups of filaments) followed by redistribution of the applied load between intact fibers rather than creep of intact fibers. However, as creep deformation is recognized to occur under these testing conditions – constant load at elevated temperature – it is illustrative to analyze the deformation as if it were due to creep. For this purpose, the strain rates extracted from the steady-state portions of the strain vs time curves obtained in this work are plotted vs the applied stress (Figure 8). The data in Figure 8 can be fitted with a general Norton-Baily power-law equation:

$$\dot{\varepsilon} = A\sigma^n \quad (12)$$

In this equation, A is a temperature-dependent coefficient, σ is the applied stress, and n is the stress exponent found in Equation 2. The value of the stress exponent n = 2.44 is readily determined from the data in Figure 10.

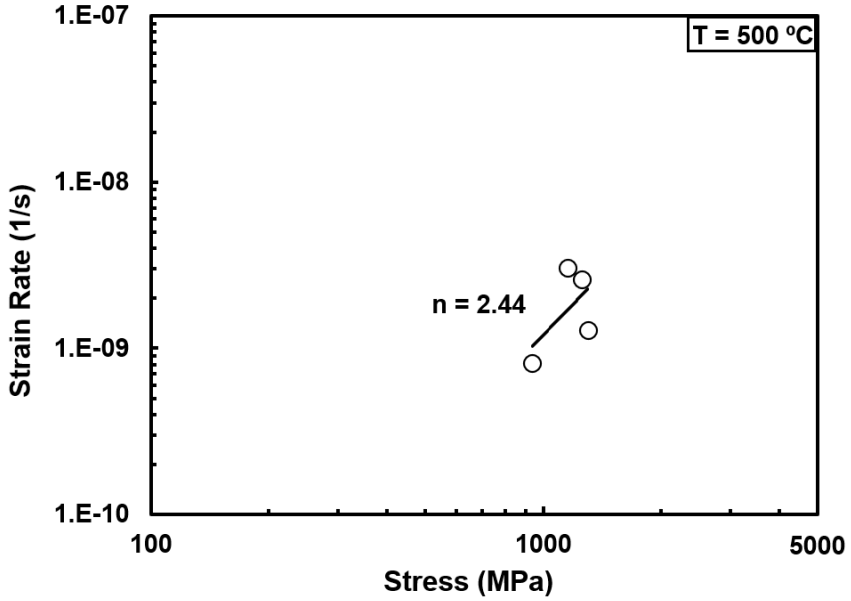

Figure 10. Steady-state strain rates vs applied stress at 500°C in air

If the deformation mechanism were creep, the calculated value of the stress exponent, 2.44, would indicate a deformation mechanism of grain boundary sliding and/or interface-controlled creep. However, at the test temperature of 500°C, it is recognized that the presence of creep deformation is likely to be negligible.

4.3 Static Fatigue in Steam

Tensile static fatigue tests in silicic acid-saturated steam were performed at 500°C for applied stresses ranging from from 3.6 MPa to 1350 MPa. Results are summarized in Table 6. Results are also presented in Figures 11 and 12, where accumulated strain is

plotted vs time. Note that in Figure 12, the time scale is reduced to highlight the strain vs time behavior during the early portion of the static fatigue test.

Table 6. Summary of Tensile Static Fatigue Tests of Hi-Nicalon^{TM} S in Saturated Steam at 500°C

Specimen	Stress (MPa)	Lifetime (hr)	Steady-state Creep Rate (1/s)	Total Strain (%)
R-22	3.6	100	1.59×10^{-11}	0.00162
C-19	1300.0	100	3.22×10^{-9}	0.242
C-18	1350.3	22.2*	1.10×10^{-8}*	0.296*

*Test terminated due to equipment malfunction

During the test conducted at 1350.5 MPa, the temperature of the steam entering the test chamber dropped from ~500°C to ~257°C after 22.2 hours had elapsed. While the furnace temperature remained constant and the test ran to the 100-hour runout, only data for the time period with the properly heated steam is considered.

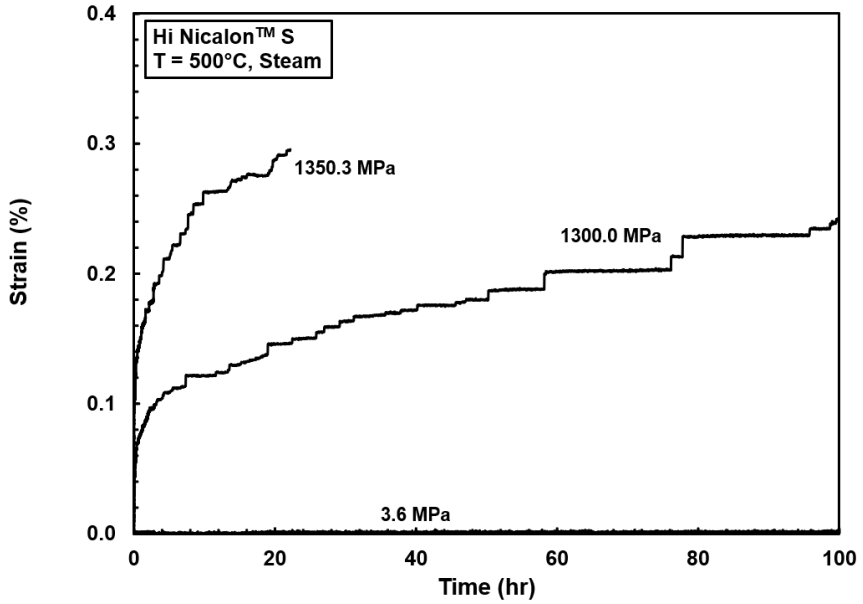

Figure 11. Strain vs time curves obtained for Hi-Nicalon™ S fiber tows at 500° C in silicic acid-saturated steam

By focusing on the initial time period under load, it is evident that steady-state strain vs time behavior had been achieved after about 0.5 h under applied stress. Thus in silicic acid saturated-steam the transition from transient to steady-state strain vs time behavior occurred earlier than in air. A similar observation by Piper [18], who studied static fatigue of Hi-Nicalon™ S fiber tows at 700°C in air and silicic acid-saturated steam. This fact explains why, despite having a steady-state strain rate an order of magnitude higher in saturated steam than in air, the final strain values produced in both environments have the same order of magnitude. It also appears that at higher applied stresses the transient strain vs time behavior lasted longer in saturated steam than in air.

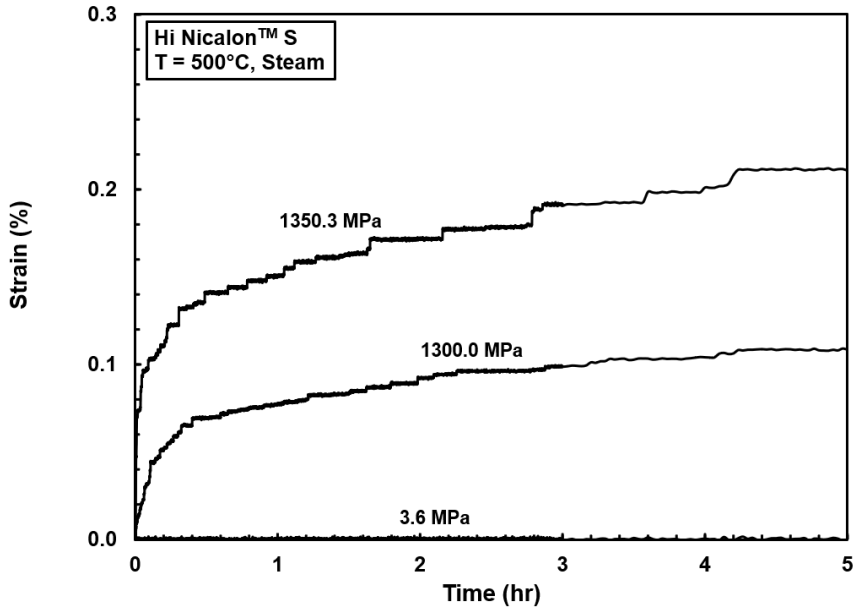

Figure 12. Strain vs time curves obtained for Hi-Nicalon™ S fiber tows at 500° C in silicic acid-saturated steam. The time scale is truncated to highlight strain vs time behavior during the first 5 h of the test.

It is of interest to compare the strain rates found by testing in saturated steam at 500°C to the rates found by testing in air at 500°C and to testing accomplished at higher temperatures. These comparisons are displayed in Figures 13 and 14. It is apparent from Figure 13 that the addition of a silicic acid-saturated steam atmosphere accelerated the steady-state strain rate of the fiber tows. It is also apparent from Figure 14 that at the temperatures shown the raising of the test temperature has a comparable, if not more significant, effect on the steady-state strain rates than the environment does.

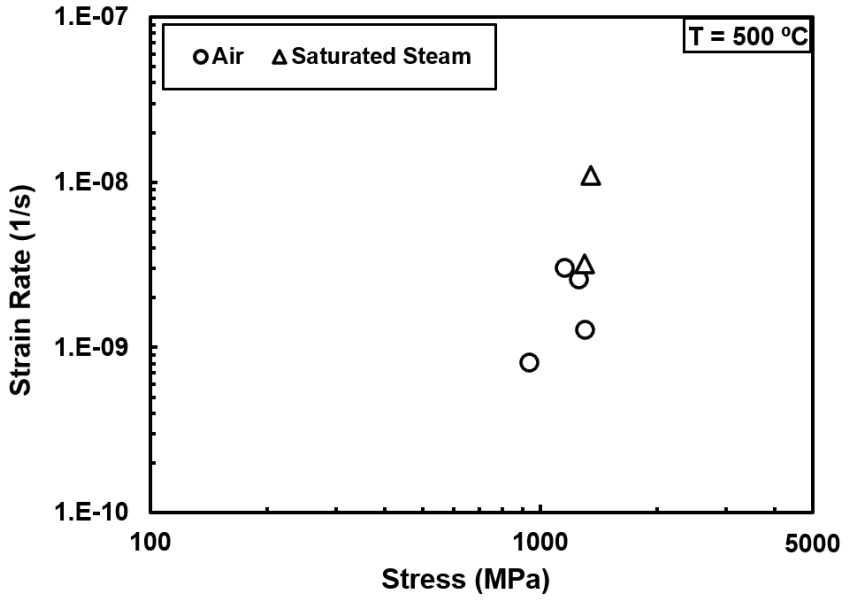

Figure 13. Steady-state strain rates vs applied stress at 500°C in air and silicic acid-saturated steam

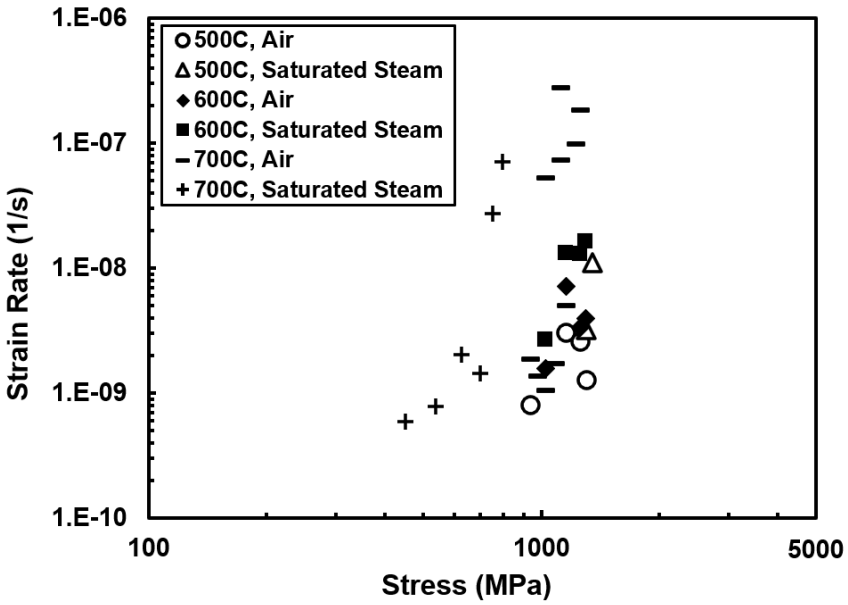

Figure 14. Steady-state strain rates vs applied stress in air and in silicic acid-saturated steam [18, 24].

It is recognized that microstructural investigation of the tested fiber tows under an SEM and TEM is necessary to gain insight into the physical deformation mechanisms. However, the experimental data also offers several different clues. In several tests, most

notably in the 1156 MPa test in air and the 1300 MPa test in saturated steam, periods of rapid strain increase are followed by periods of relatively constant strain. These “jumps” in strain are indicative of progressive fiber failure – a fiber or a group of fibers fail, with the applied stress then being redistributed between the remaining intact fibers. Still it is possible that this deformation mechanism operates in addition to creep deformation.

V Conclusions and Recommendations

5.1 Conclusions

The static fatigue behavior of Hi-Nicalon™ S fiber tows was investigated at 500°C in laboratory air and in silicic acid-saturated steam. All test specimens survived 100 h under applied stress without failure prior to run-out. Strain accumulation was measured in each test. Strain vs time behavior exhibited two regimes: an initial transient regime followed by the steady-state regime. Steady-state strain rates were extracted from the strain vs time curves. Strain rates in silicic acid-saturated steam were an order of magnitude higher than those in air, although final strain values upon run-out were comparable.

5.2 Future Research Recommendations

Due to outside constraints, imaging of the specimens tested in air and steam could not be carried out. This imaging is important in order to identify the deformation mechanism and understand the nature of the oxidation caused by the silicic acid-saturated steam. Post-test tow microstructure should be analyzed via both scanning electron microscopy (SEM) and transmission electron microscopy (TEM. The tested specimens have been saved for this purpose. While the stress-strain-temperature data collected suggest less of an oxidation impact than previously seen at higher temperatures, this can only be verified through SEM and/or TEM microscopy.

Static fatigue testing of Hi-Nicalon™ S fiber tows in air and silicic acid-saturated steam has been conducted at temperatures ranging from 500°C to 1100°C. It would be beneficial to perform similar at still higher temperatures. Modification of the furnace

and/or steam generation system may be necessary to accomplish such testing in a predictable manner. Preliminary attempts made early in this research effort to obtain a stable test environment at 1200°C were not successful. As encountered in this research effort, the current furnace heating elements were not well suited for testing at temperatures in excess of 1100°C and failed shortly after reaching higher temperatures.

It would also be useful to analyze a full SiC-SiC CMC reinforced with Hi-Nicalon™ S fibers under load at elevated temperature in a steam environment. Silicic acid-saturated steam was used in this effort because it has been demonstrated that unsaturated water leached silicon species from the SiC fibers [17] in a manner that unsaturated steam would leach species from the SiC matrix prior to reaching the fibers. This assumption can then be tested in a more representative configuration, and the any impacts of the matrix having its silicon leached from it can be incorporated into the analysis.

Appendix: Cold Start Procedures

1. Confirm the water barrel contains at least several inches of deionized water, and the flexible tube is inserted into the water.
2. Check that all power switches for equipment on the cart are switched off.
3. Flip the light switch underneath the LVDT on.
4. Check water pump operation
    a. Disconnect water hose from steam generator.
    b. Press the water pump controller's "START" button
    c. Wait a few seconds to confirm water is flowing from barrel through hose.
    d. Turn off the water pump controller.
    e. Reconnect water hose to steam generator.
5. Check steam generator operation
    a. Loosen the three eye nuts attaching the steam generator to the preheater and carefully separate the two, taking care not to pull on or impact the ceramic tube inside the preheater.
    b. Switch on the steam generator voltage control box (on the cart's middle shelf) and turn on the water pump.
    c. Confirm the "snout temperature" thermocouple reading is rising.
    d. Wait a minute longer and confirm steam is visibly exiting the steam generator.
    e. Power the steam generator and water pump off.
6. Check preheater assembly
    a. Remove the insulation from the exterior of the preheater, taking care not to jostle the braids or posts protruding from the insulation blocks.

b. Confirm the heating coils are intact and wired in series, and the braids are intact and not touching the metal sides of the preheater.
c. Confirm the preheater's thermocouple fully inserted through the insulation block and connected to the preheater temperature control box.
d. Remove the loose silica wool from inside the ceramic tube.
e. Loosely pack new silica wool into the tube, making sure not to produce a "plug" of wool at any point which would obstruct the flow of steam toward the furnace.
f. Re-assemble the preheater and replace insulation wool on top, replacing any deteriorated pieces.

7. Check preheater operation
    a. Switch on the preheater temperature control box on the cart's bottom shelf.
    b. Set temperature control to the temperature of interest.
    c. Press the "ON" button on the temperature control box ("ON" button will not illuminate, but the "OFF" button will not be glowing red).
    d. Wait several minutes to ensure the temperature in the preheater is climbing.
    e. Power off the preheater.
    f. Wait for the preheater to return to room temperature.
    g. Reconnect the steam generator to the preheater, replacing the insulation washer if the existing one is deteriorated.
8. Turn on the water pump, steam generator, and preheater, and set to the desired setting.

9. Check the temperature indications from the steam generator and preheater thermocouples to ensure proper operation.
10. Visibly confirm steam being expelled through preheater.
11. Power everything off.
12. Check the thermocouple in the steam outlet tube to ensure proper operation and calibration.
13. Check furnace operation and assembly
    a. Visibly check the two furnace halves are installed correctly and aligned.
    b. Visibly confirm two thermocouples inserted into right-hand half of furnace and all four heating elements are in place and intact.
    c. With the furnace open, use the MTS software to set the temperatures in the top and bottom zones to 100°C.
    d. Visibly confirm all four heating elements glow and the temperature readings for both zones are climbing properly.
    e. Shut down the furnace and allow it to return to room temperature.
    f. Visibly inspect the furnace's insulation blocks for cracks or deterioration, carving new blocks to fit if necessary.

Bibliography

[1] W. F. Smith, *Principles of Materials Science and Engineering*, 3rd ed. New York: McGraw-Hill, Inc, 1996

[2] K. K. Chawla, *Ceramic Matrix Composites*. New York: Springer, 1998.

[3] I. M. Daniel and O. Ishai, *Engineering Mechanics of Composite Materials*, 2nd ed. New York: Oxford University Press, 2006.

[4] W. Durant, *The Story of Civilization Part I: Our Oriental Heritage*, New York: Simon & Schuster, 1935

[5] T. L. Anderson, *Fracture Mechanics*, 3rd ed. Boca Raton: Taylor & Francis Group, 2005

[6] C. J. Armani, "Creep Performance of Oxide Ceramic Fiber Materials at Elevated Temperature in Air and in Steam," Air Force Institute of Technology (AU), 2011.

[7] N. P. Bansal and J. Lamon, *Ceramic Matrix Composites: Materials, Modeling and Technology*, , Eds. John Wiley & Sons, Inc., 2015.

[8] F. W. Zok, "Developments in Oxide Fiber Composites," *J. Am. Ceram. Soc.*, vol 89, no. 11, pp. 3309-3324, Nov. 2006.

[9] W. Gauthier and J. Lamon, "Delayed Failure of Hi-Nicalon and Hi-Nicalon S Multifilament Tows and Single Filaments at Intermediate Temperatures (500°-800°C)," *J. Am. Ceram. Soc.*, vol. 92, no. 3, pp. 702–709, Mar. 2009.

[10] T. Ishikawa, "Advances in Inorganic Fibers," *Polym. Inorg. Fibers*, vol. 178, pp. 109–144, 2005.

[11] A. Bunsell and A. Piant, "A review of the development of three generations of small diameter silicon carbide fibres," *J. Mater. Sci.*, vol. 41, pp. 823–839, 2006.

[12] N. E. Dowling, S. L. Kampe, and M. V. Kral, *Mechanical Behavior of Materials*, 5th ed. United Kingdom: Pearson Educated Limited, 2019

[13] I. H. Shames and F. A. A. Cozzarelli, *Elastic and Inelastic Stress Analysis*. Philadelphia: PA: Taylor & Francis Group, 1997.

[14] S. J. Robertson, "Creep of Hi-Nicalon S Ceramic Fiber Tows at 800 deg C in Air and in Silicic Acid-Saturated Steam," Air Force Institute of Technology (AU), 2015.

[15] J. Wachtman, W. Cannon, and M. Matthewson, *Mechanical Properties of Ceramics*, 2nd ed. New York: John Wiley & Sons, Inc., 2009.

[17] T. R. Shillig, "Creep of Hi-Nicalon S Fiber Tows at Elevated Temperature in Air and in Steam," Air Force Institute of Technology (AU), 2013.

[18] M. W. Piper, "Creep of Hi-Nicalon S Ceramic Fiber Tows at 700°C Elevated Temperature in Air and in Silicic Acid-Saturated Steam," Air Force Institute of Technology (AU), 2016.

[19] R. K. Mitchell, "Creep of Hi-Nicalon S Ceramic Fiber Tows at 900°C Elevated Temperature in Air and in Silicic Acid-Saturated Steam," Air Force Institute of Technology (AU), 2017.

[20] B. G. Kroeger, "Creep of Hi-Nicalon S Ceramic Fiber Tows at 1000°C in Air and in Silicic Acid-Saturated Steam," Air Force Institute of Technology (AU), 2018.

[21] L. M. Gumucio, "Creep of Hi-Nicalon S Ceramic Fiber Tows at 1100°C in Air and in Silicic Acid-Saturated Steam," Air Force Institute of Technology (AU), 2018

[22] COI Ceramics, "HI-NICALON™ TYPE S CERAMIC FIBER" *ATK Space Systems Inc.* [Online]. Available: http://www.coiceramics.com/pdfs/hi-nicalon-types_1-17-06.pdf. [Accessed: 18-January-2021].

[23] NGS Advanced Fiber Co., "Product NGS Advanced Fibers," *NGS Advanced Fiber Co., Ltd*, 2017. [Online]. Available: http://www.ngs-advanced-fibers.com/eng/item/index.html. [Accessed: 09-February-2021].

[24] C. Nelson, "Static Fatigue of Hi-Nicalon S Ceramic Fiber Tows at 600°C in Air and in Silicic Acid-Saturated Steam," Air Force Institute of Technology (AU), 2021.

REPORT DOCUMENTATION PAGE		Form Approved OMB No. 0704–0188

1. REPORT DATE (DD–MM–YYYY)	2. REPORT TYPE	3. DATES COVERED *(From — To)*
25-03-2021	Master's Thesis	OCT 20 – FEB 21

4. TITLE AND SUBTITLE	5a. CONTRACT NUMBER
Static Fatigue of Hi-Nicalon S Fiber Tows at 500C in Air and in Silicic Acid-Saturated Steam	5b. GRANT NUMBER
	5c. PROGRAM ELEMENT NUMBER
6. AUTHOR(S) Reinink, Richard J., Capt, USAF	5d. PROJECT NUMBER
	5e. TASK NUMBER
	5f. WORK UNIT NUMBER

7. PERFORMING ORGANIZATION NAME(S) AND ADDRESS(ES)	8. PERFORMING ORGANIZATION REPORT NUMBER
Air Force Institute of Technology Graduate School of Engineering and Management (AFIT/ENY) 2950 Hobson Way WPAFB OH 45433-7765	AFIT-GMS-ENY-21-M-315
9. SPONSORING / MONITORING AGENCY NAME(S) AND ADDRESS(ES) Air Force Research Laboratory Dr Randall S. Hay, 2977 Hobson Way, Building 652 Wright-Patterson AFB, OH 45433 Randall.hay@us.af.mil	10. SPONSOR/MONITOR'S ACRONYM(S) AFRL/RXCCM
	11. SPONSOR/MONITOR'S REPORT NUMBER(S)

12. DISTRIBUTION / AVAILABILITY STATEMENT
APPROVED FOR PUBLIC RELEASE; DISTRIBUTION UNLIMITED

13. SUPPLEMENTARY NOTES
This material is declared a work of the U.S. Government and is not subject to copyright protection in the United States.

14. ABSTRACT

Recent developments in aerospace propulsion systems, along with emerging interest in hypersonic air vehicles has emphasized the need for materials which can withstand extreme service environments. The leading candidates for the structural components expected to operate in these environments are SiC-based ceramic matrix composites (CMCs). When a CMC component is subjected to thermomechanical loads in an aggressive environment during service, surface cracks form. As steam penetrates cracks in the SiC matrix, it becomes saturated with silicic acid, ($SI(OH)_4$) and attacks the SiC fibers. The interaction between the Hi-Nicalon™ S SiC fibers and the $Si(OH)_4$)-saturated steam is not fully understood, and is essential to predicting long-term durability and assuring structural integrity of SiC/SiC CMCs.

This research effort focused on static fatigue of Hi-Nicalon™ S fiber tows at 500°C in air and in silicic acid-saturated steam. The fiber tows were composed of 500 fiber filaments with an average diameter of 12 μm. The applied stress ranged from 3.6 MPa to 1350 MPa. Both primary and secondary deformation regimes were observed, and steady-state strain rates were found for each test. The effects of applied load and test environment on static fatigue performance of the SiC fiber tow are discussed.

15. SUBJECT TERMS
Hi-Nicalon™-S, SiC fiber tows, ceramic fibers, creep, tension, steam environment, static fatigue

16. SECURITY CLASSIFICATION OF:			17. LIMITATION OF ABSTRACT	18. NUMBER OF PAGES	19a. NAME OF RESPONSIBLE PERSON
a. REPORT	b. ABSTRACT	c. THIS PAGE	UU	53	Dr. Marina Ruggles-Wrenn
U	U	U			19b. TELEPHONE NUMBER (Include Area Code) (937) 255-3636, ext 4641 Email: marina.ruggles-wrenn@afit.edu